

1 Quantifying the migration rate of drainage divides from 2 high-resolution topographic data

3 Chao Zhou¹, Xibin Tan^{2,*}, Yiduo Liu², Feng Shi^{1,3}

4 ¹ State Key Laboratory of Earthquake Dynamics, Institute of Geology, China
5 Earthquake Administration, Beijing 100029, China

6 ² Key Laboratory of Mountain Hazards and Surface Processes, Institute of Mountain
7 Hazards and Environment, Chinese Academy of Sciences, Chengdu 610299, China

8 ³ Shanxi Taiyuan Continental Rift Dynamics National Observation and Research
9 Station, Beijing 100029, China

10 *Corresponding author. E-mail address: tanxibin@imde.ac.cn

11 Abstract

12 The lateral movement of drainage divides is co-influenced by tectonics,
13 lithology, and climate, and therefore archives a wealth of geologic and climatic
14 information. It also has wide-ranging implications for topography, sedimentary
15 record, and biological evolution, thus has drawn much attention in recent years.
16 Several methods have been proposed to determine the drainage divide's migration
17 state (direction and rate), including geochronological approaches (e.g., ¹⁰Be) and
18 topography-based approaches (e.g., χ -plots or Gilbert metrics). A key object in these
19 methods is the channel head, which separates the hillslope and channel. However, due
20 to the limited resolution of topography data, the required channel-head parameters in
21 the calculation often cannot be determined accurately, and empirical values are used

22 in the calculation, which may induce uncertainties. Here, we propose two methods to
23 calculate the migration rate of drainage divides, based on the relatively accurate
24 channel-head parameters derived from high-resolution topographic data. We then
25 apply the methods to an active rift shoulder (Wutai Shan) in the Shanxi rift, and a
26 tectonically stable area (Yingwang Shan) in the Loess Plateau, to illustrate how to
27 calculate drainage-divide migration rates. Our results show that the Wutai Shan
28 drainage divide is migrating northwestward at a rate between 0.21 to 0.27 mm/yr,
29 whereas the migration rates at the Yingwang Shan are approximately zero. This study
30 indicates that the drainage-divide stability can be determined more accurately using
31 high-resolution topographic data. Furthermore, this study takes the cross-divide
32 differences in the uplift rate of channel heads into account in the measurement of
33 drainage-divide migration rate for the first time.

34 **Keywords**

35 Drainage divide; Migration rate; High-resolution topographic data; DEM; Channel
36 head

37 **1. Introduction**

38 The evolution of the Earth's surface is jointly controlled by tectonics, lithology,
39 and climatic conditions (e.g., [Molnar and England, 1990](#); [Whipple, 2009](#); [Gallen,](#)
40 [2018](#); [Bernard et al., 2021](#); [Hoskins et al., 2023](#)), providing a basis for reconstructing
41 the past tectonic ([Pritchard et al., 2009](#); [Kirby et al., 2012](#); [Shi et al., 2021](#)) or climatic

42 processes (Tucker et al., 1997; Hancock et al., 2002; Schildgen et al., 2022) through
43 topography. The evolution of unglaciated terrestrial terrains is fundamentally coupled
44 with changes in drainage systems through river's vertical (changes in river long
45 profile) and lateral movements (drainage divide migration and river captures)
46 (Whipple, 2001; Clark et al., 2004; Bonnet, 2009; Willett et al., 2014). Previous
47 studies have extensively investigated how river channel profiles respond to tectonic
48 uplift (Whipple, 2001; Crosby and Whipple, 2006; Kirby et al., 2012), lithological
49 difference (Duvall et al., 2004; Safran et al., 2005; Forte et al., 2016), and
50 precipitation perturbations (Schlunegger et al., 2011; Bookhagen and Strecker, 2012).
51 River's long profiles have been used to study the earthquake events (e.g., Burbank and
52 Anderson, 2001; Wei et al., 2015) and the spatio-temporal variations of uplift (e.g.,
53 Whipple et al., 1999; Kirby et al., 2003; Pritchard et al., 2009; Goren et al., 2014).
54 Recent studies show that the widespread lateral movement of river basins driven by
55 geological and/or climatic disturbance (Yang et al., 2019; Zondervan et al., 2020;
56 Zhou et al., 2022a; Bian et al., 2024) also interacts with the adjustment of channel
57 profiles (Willett et al., 2014). Drainage-divide migration, one form of river lateral
58 movement, may not only carry information on geological and/or climatic disturbance
59 (Su et al., 2020; Zondervan et al., 2020; He et al., 2021; Shi et al., 2021; Zhou et al.,
60 2022a; Zeng and Tan, 2023) but also influence the extraction of tectonic information
61 from channel profiles (Goren et al., 2014; Ma et al., 2020; Jiao et al., 2021).
62 Moreover, it has multi-facet consequences for landscape evolution (Scheingross et al.,
63 2020; Stokes et al., 2022), sedimentary processes (Clift & Blusztajn, 2005; Willett et

64 al., 2018; Deng et al., 2020; Zhao et al., 2021), and biological evolution (Waters et al.,
65 2001; Zemplak et al., 2008; Hoorn et al., 2010; Musher et al., 2022). For this reason,
66 the stability of drainage divides has drawn more and more attention in recent years
67 (e.g., Authemayou et al., 2018; Vacherat et al., 2018; Chen et al., 2021; Shelef and
68 Goren, 2021; Sakashita and Endo, 2023; Bian et al., 2024).

69 Drainage-divide migration is essentially controlled by the cross-divide
70 difference in erosion and topographic slope (Beeson et al., 2017; Dahlquist et al.,
71 2018; Chen et al., 2021; Zhou et al., 2022a). The erosion rates are routinely derived
72 from geochronological techniques, such as cosmogenic nuclides (e.g., ^{10}Be)
73 concentration measurements (Mandal et al., 2015; Struth et al., 2017; Sassolas-
74 Serrayet et al., 2019), which can be used to calculate the migration rates of drainage
75 divides (Beeson et al., 2017; Godard et al., 2019; Hu et al., 2021). However, these
76 techniques are usually based on samples collected from a catchment outlet that is
77 several, or even tens of, kilometers away from the drainage divide and thus may not
78 represent the erosion rates close to the drainage divide (Sassolas-Serrayet et al., 2019;
79 Zhou et al., 2022a). Besides, the high cost of sample processing makes it challenging
80 to determine the drainage divide's motion by measuring the erosion rates throughout
81 the large landscapes. Hence, it would be ideal to find an accessible and efficient
82 method that can be applied to the entire landscape and make full use of the ^{10}Be -
83 derived erosion rates.

84 The advancement of the digital elevation model (DEM) has promoted the
85 development of geomorphic analysis, making it possible to determine the drainage

86 divide's transient motion through topography analysis. For example, Willett et al.
87 (2014) applied the χ method to map the dynamic state of river basins. Forte and
88 Whipple (2018) proposed the cross-divide comparison of "Gilbert metrics" (including
89 channel heads' relief, slope, and elevation) to determine a drainage divide's migration
90 direction. Others adopted the comparison of slope angle or relief of the hillslopes
91 across a drainage divide to deduce its stability (Scherler and Schwanghart, 2020; Ye et
92 al., 2022; Zhou et al., 2022b). These geomorphic techniques, so far, could only
93 determine the migration direction of drainage divides. Braun (2018) provided an
94 equation that considers both alluvial and fluvial areas to calculate the migration
95 velocity of an escarpment (also a drainage divide). Zhou et al. (2022a) developed a
96 technique to calculate the migration rate through the high base-level χ values on both
97 sides of a drainage divide. These new approaches require channel-head parameters to
98 calculate the migration rate. However, the location of the channel heads sometimes
99 cannot be accurately identified because of the limitation in the resolution of DEMs in
100 natural cases. For this reason, empirical values of channel-head parameters are used in
101 these studies, which may induce uncertainties.

102 This study aims to establish an approach to derive the migration rate of drainage
103 divides, at a high precision and low cost, based on topographic analysis. We choose a
104 tectonically active area (i.e., the Wutai Shan in the Shanxi Rift) and a tectonically
105 inactive area (i.e., the Yingwang Shan in the Loess Plateau) to demonstrate how to
106 quantify drainage-divide migration rates (Fig. 1). We use the aerial photography
107 acquired by unmanned aerial vehicles (UAVs) and the Structure from Motion (SfM)

108 technology to obtain the high-resolution DEM data of these two areas (0.67 m and
109 0.84 m spatial resolution in the Wutai Shan and the Yingwang Shan, respectively).
110 Benefiting from the high-resolution data, the location of channel heads can be
111 identified more accurately. We then develop two methods to calculate the drainage-
112 divide migration rates. One is based on the measured channel-head parameters, and
113 the other is based on an improved method of Zhou et al (2022a). Combining with the
114 geological and low-temperature thermochronology studies of the Wutai Shan
115 (Middleton et al., 2017; Clinkscales et al., 2020), we also quantify the cross-divide
116 difference in uplift rates to improve the precision of drainage-divide migration rate.
117

118 **2. Methods**

119 **2.1 Channel-head-point method**

120 According to the detachment-limited stream power model (Howard and Kerby,
121 1983; Howard, 1994), the channel's erosion rate (E) can be expressed as:

$$122 \quad E = KA^m S^n \quad (1)$$

123 where K is the erosion coefficient, A is the upstream drainage area, S is the gradient of
124 the river channel, and m and n are empirical constants.

125 Because of thresholds such as erosion threshold (the shear stress of overland flow
126 must exceed the threshold of the cohesion of bed material to generate river incision)
127 (Howard and Kerby, 1983; Perron et al., 2008) or landslide threshold (landslides
128 occur when the threshold of soil or rock strength is exceeded in high relief region)

129 (Burbank et al., 1996; Tucker et al., 1998), river channels (following Eq. 1) emerge at
130 a certain distance from the drainage divide. The region between the channel head and
131 the drainage divide is referred to as the hillslope area, where the erosion is controlled
132 by landslide, collapse, and diffusion processes (Stoke and Dietrich, 2006; Stark, 2010;
133 Braun et al., 2018; Dahlquist et al., 2018). The channel-head point is the highest and
134 the closest point to the drainage divide on a river channel (Clubb et al., 2014).

135 Therefore, the erosion rate at channel-head points (E_{ch}) can be described as:

$$136 \quad E_{ch} = KA_{cr}^m S_{ch}^n \quad (2)$$

137 where E_{ch} is the erosion rate at channel-head points, A_{cr} is the critical upstream
138 drainage area of a channel-head point (Duvall et al., 2004; Wobus et al., 2006), and
139 S_{ch} is the channel-head gradient measured along the channel near the channel-head
140 point. Eq. 2 indicates that the side of a drainage divide with a higher A_{cr} or S_{ch} can
141 have a higher erosion rate than the other side, and is more likely to pirate the opposite
142 drainage basin. Besides, a high erosion coefficient can amplify the drainage basin's
143 erosion rate.

144 Drainage-divide migration is essentially controlled by the cross-divide difference
145 in erosion rates and topographic slope (Beeson et al., 2017; Dahlquist et al., 2018;
146 Chen et al., 2021; Zhou et al., 2022a; Stokes et al., 2022). Furthermore, the
147 differential uplift should also be considered when using the cross-divide erosion rates
148 at the channel heads to calculate the erosion difference across the divide, especially in
149 the case of tectonic tilting uplift (Zhou et al., 2022a). The drainage-divide migration
150 rate (D_{mr}) can be obtained according to the cross-divide difference in erosion rate and

151 uplift rate and the slopes across the divide (Zhou et al., 2022a):

$$152 \quad D_{mr} = \frac{\Delta E_{ch} - \Delta U_{ch}}{\tan\alpha + \tan\beta} \quad (3)$$

153 where ΔE_{ch} is the difference in erosion rate between the two sides (annotated as α and
 154 β) of the drainage divide ($\Delta E_{ch} = E_{ch\alpha} - E_{ch\beta}$). The choice of α or β is arbitrary, and the
 155 positive direction of the migration rate is assigned from the α to the β side whereas the
 156 negative is the opposite. ΔU_{ch} is the cross-divide difference in uplift rate ($\Delta U_{ch} = U_{ch\alpha}$
 157 $- U_{ch\beta}$), and $\tan\alpha$ and $\tan\beta$ are the gradients on each side of the drainage divide.

158 Assuming erosion coefficient (K) is the same on both sides of a drainage divide, Eqs.
 159 2 and 3 allow us to derive the equation of drainage divide's migration rate according
 160 to the parameters at the channel-head points:

$$161 \quad D_{mr} = \frac{K[(A_{cr}^m S_{ch}^n)_\alpha - (A_{cr}^m S_{ch}^n)_\beta] - \Delta U_{ch}}{\tan\alpha + \tan\beta} \quad (4)$$

162 If the exact value of K is unknown, the drainage divide's unilateral erosion rate
 163 can be used as a substitution:

$$164 \quad D_{mr} = \frac{E_\alpha \left[1 - \frac{(A_{cr}^m S_{ch}^n)_\beta}{(A_{cr}^m S_{ch}^n)_\alpha} \right] - \Delta U_{ch}}{\tan\alpha + \tan\beta} \quad (5)$$

165 or:

$$166 \quad D_{mr} = \frac{E_\beta \left[\frac{(A_{cr}^m S_{ch}^n)_\alpha}{(A_{cr}^m S_{ch}^n)_\beta} - 1 \right] - \Delta U_{ch}}{\tan\alpha + \tan\beta} \quad (6)$$

167 E_α and E_β are the erosion rates of the α and the β side of the drainage divide,
 168 respectively, which can be derived through cosmogenic nuclides (^{10}Be) concentration
 169 measurements (Beeson et al., 2017; Godard et al., 2019; Hu et al., 2021). The regional
 170 average erosion rate ($\bar{E} = \frac{E_\alpha + E_\beta}{2}$) can also be used to calculate the migration rate:

$$D_{mr} = \frac{2\bar{E} \left[\frac{(A_{cr}^m S_{ch}^n)_\alpha - (A_{cr}^m S_{ch}^n)_\beta}{(A_{cr}^m S_{ch}^n)_\alpha + (A_{cr}^m S_{ch}^n)_\beta} \right] - \Delta U_{ch}}{\tan\alpha + \tan\beta} \quad (7)$$

Based on Eqs. 4-7, the migration rate of drainage divides can be estimated using channel-head parameters combined with one of the erosion-related parameters, erosion coefficient (K), erosion rate at one side of a drainage divide (E_α or E_β), or regional average erosion rate (\bar{E}).

2.2 Channel-head-segment method

A channel-head segment is the channel segment just below the channel head (Zhou et al., 2022a). Zhou et al. (2022a) developed a method based on the cross-divide χ contrast of channel-head segments to calculate the migration rate of drainage divides. The essence of the method is the cross-divide comparison of the channel-head segments' normalized channel steepness (k_{sn}) values. k_{sn} is a widely used index (Whipple et al., 1999; Wobus et al., 2006; Hilley and Arrowsmith, 2008; Kirby and Whipple, 2012) that is quantitatively related to E and K ($k_{sn} = \left(\frac{E}{K}\right)^{\frac{1}{n}}$). χ is an integral function ($\chi = \int_{x_b}^x \left(\frac{A_0}{A(x)}\right)^{\frac{m}{n}} dx$) of a channel's upstream area (A) to horizontal distance (x) (Royden et al., 2000; Perron and Royden, 2012), and A_0 is an arbitrary scaling area to make the integrand dimensionless.

In the method of Zhou et al. (2022a), the location of channel heads cannot be accurately identified, because it is limited by the resolution of DEM. Therefore, an empirical value of $A_{cr} = 10^5 \text{ m}^2$ was used in the calculation. Benefiting from the high-resolution DEM in this study, we improve the method in Zhou et al. (2022a) and use

192 the real location of channel heads to calculate the migration rate. When the regional
 193 erosion coefficient (K) is known and unchanged in the vicinity of the drainage divide,
 194 the drainage-divide migration rate can be estimated by the following equation:

$$195 \quad D_{mr} = \frac{K[k_{sn(\alpha)}^n - k_{sn(\beta)}^n] - \Delta U_{ch}}{\tan\alpha + \tan\beta} = \frac{K \left\{ \left[\frac{(z_{ch} - z_b)_\alpha}{\chi_\alpha} \right]^n - \left[\frac{(z_{ch} - z_b)_\beta}{\chi_\beta} \right]^n \right\} - \Delta U_{ch}}{\tan\alpha + \tan\beta} \quad (8)$$

196 where z_{ch} and z_b are the elevations of the channel heads and catchment outlets,
 197 respectively. The detailed derivation of Eq. 8 is in Supplementary Materials. The
 198 drainage divide's unilateral erosion rate (E_α or E_β) can also be used as a substitution
 199 for the K value:

$$200 \quad D_{mr} = \frac{E_\alpha \left\{ 1 - \left(\frac{\chi_\alpha}{\chi_\beta} \right)^n \left[\frac{(z_{ch} - z_b)_\alpha}{(z_{ch} - z_b)_\beta} \right]^{-n} \right\} - \Delta U_{ch}}{\tan\alpha + \tan\beta} \quad (9)$$

201 or:

$$202 \quad D_{mr} = \frac{E_\beta \left\{ \left(\frac{\chi_\alpha}{\chi_\beta} \right)^{-n} \left[\frac{(z_{ch} - z_b)_\alpha}{(z_{ch} - z_b)_\beta} \right]^n - 1 \right\} - \Delta U_{ch}}{\tan\alpha + \tan\beta} \quad (10)$$

203 Alternatively, one can use the regional average erosion rate (\bar{E}) to calculate the
 204 migration rate:

$$205 \quad D_{mr} = \frac{2\bar{E} \left\{ \frac{\left[\frac{(z_{ch} - z_b)_\alpha}{(z_{ch} - z_b)_\beta} \right]^n - \left(\frac{\chi_\alpha}{\chi_\beta} \right)^n}{\left[\frac{(z_{ch} - z_b)_\alpha}{(z_{ch} - z_b)_\beta} \right]^n + \left(\frac{\chi_\alpha}{\chi_\beta} \right)^n} \right\} - \Delta U_{ch}}{\tan\alpha + \tan\beta} \quad (11)$$

206 Based on Eqs. 8-11, the drainage-divide migration rate can be estimated using the χ
 207 values of high-base-level channel segments combined with one of the erosion-related
 208 parameters, erosion coefficient (K), erosion rate at one side of a drainage divide (E_α or
 209 E_β), or regional average erosion rate (\bar{E}).

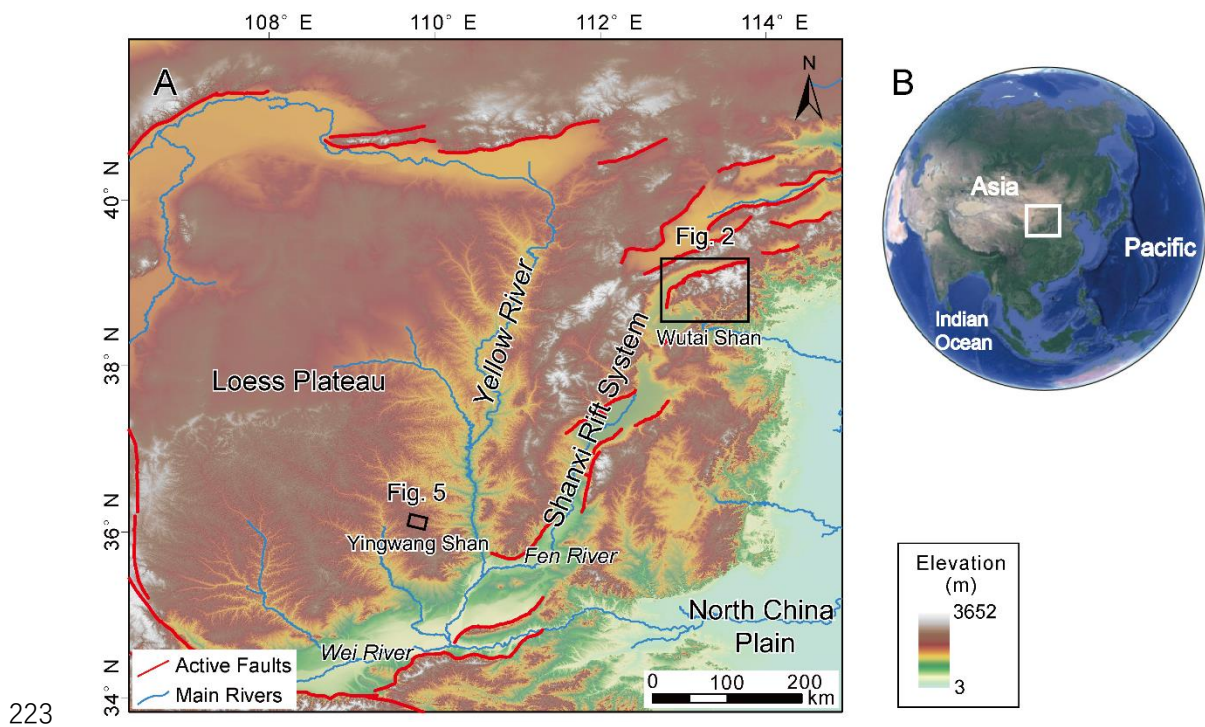
210 We use UAV-acquired aerial photography and structure from motion (SfM)

211 photogrammetry to derive the high-resolution DEM of the two study areas, the Wutai
212 Shan in the Shanxi Rift, and the Yingwang Shan in the Loess Plateau, both located in
213 North China (Fig. 1). The spatial resolution is 0.67 m in the Wutai Shan, and 0.84 m
214 in the Yingwang Shan. Based on the high-resolution topography data, we extract the
215 relevant parameters and calculate the drainage-divide migration rate using the two
216 methods above for each case. Analysis of the data is based on the Matlab toolbox
217 TAK (Forte and Whipple, 2019) and TopoToolbox (Schwanghart and Scherler, 2014).

218

219 3. Applications to natural cases

220 We apply the new methods to two natural examples in North China, the Wutai
221 Shan in the Shanxi Rift and the Yingwang Shan in the Loess Plateau, to demonstrate
222 how to calculate the drainage-divide migration rates (Fig. 1).



223

224 **Figure 1.** Locations and tectonic background of the two nature cases in North China.
225 The figure is modified from Fig. 7 in Shi et al. (2021). (A) Red lines represent the
226 main active faults. Black rectangles show the locations of the two nature cases. Red
227 curve denotes active fault, sourced from <https://www.activefault-datacenter.cn/>. The
228 topography data (ALOS DEM, 12.5 m resolution) is downloaded from the Alaska
229 Satellite Facility (ASF) Data Search (<https://search.asf.alaska.edu/>). (B) The satellite
230 image downloaded from Google Earth. White rectangles show the location of Panel
231 A.

232

233 **3.1 Wutai Shan**

234 The Wutai Shan is a tilted fault block on the shoulder of the Shanxi Rift System
235 located in the central North China craton (Fig. 1) (Xu et al., 1993; Su et al., 2021).
236 The tilting uplift of the Wutai Shan is controlled by the Northern Wutai Shan fault,
237 and there is no active fault along the south edge of the Wutai Shan horst (Fig. 2). The
238 bedrock of the Wutai Shan area consists mainly of metamorphic and igneous
239 basement rocks (Clinkscales et al., 2020) and there is no obvious variation in rock
240 erodibility and precipitation in this area (Fig. S2 & S3). Zhou et al. (2022b) reveal that
241 the Wutai Shan drainage divide is migrating northwestward due to the tilting uplift
242 and predicts the drainage divide will move ~10 km to the northwest to achieve a
243 steady state if all geological conditions remain. Geomorphic evidence also exhibits a
244 northwestward migration of the drainage divide (Fig. 3). The plan and satellite views

245 show several barbed tributaries and a captured area around the Wutai Shan drainage
246 divide, which indicate that the tributaries formerly part of the northern drainage have
247 become part of the southern drainage (Fig. 3A&B). The χ -plots analysis shows the
248 southern side of the drainage divide has steeper channels, higher k_{sn} , and lower χ . The
249 χ -plots of paired rivers illustrate obvious characteristics of shrinking-expanding and
250 captured-beheaded rivers (Fig. 3C).

251 To derive the erosion coefficient of the Wutai Shan area, we calculate the
252 channel steepness (k_{sn}) of this region, assuming $n = 1$ and $m = 0.45$ (Wobus et al.,
253 2006; DiBiase et al., 2010; Perron and Royden, 2012; Wang et al., 2021). We then use
254 the Kriging interpolation method to generate the k_{sn} distribution map (Fig. 2B). In
255 addition, results under the assumptions of $m = 0.35$ and 0.55 , respectively, are shown
256 in Supplementary Materials (Fig. S4). The average k_{sn} value of the upthrown side near
257 the Northern Wutai Shan fault is $\sim 80 \text{ m}^{0.9}$ (Fig. 2D). Previous geological study shows
258 that the Quaternary throw rates of the Northern Wutai Shan fault are 0.8-1.6 mm/a
259 (Middleton et al., 2017). The low-temperature thermochronology study shows that the
260 time-averaged long-term throw rates in the late Cenozoic is about 0.25 mm/yr, and
261 there is an accelerated activity in the Wutai Shan area (Clinkscapes et al., 2020).
262 According to these studies, we assume a 0.50 ± 0.25 mm/yr uplift/erosion rate in the
263 northern margin of the Wutai Shan (in the footwall of the Northern Wutai Shan fault).
264 Combining with the equation, $K = \frac{E}{k_{sn}^n}$, and following the approach of previous
265 studies (Kirby and Whipple, 2001; Kirkpatrick et al., 2020; Ma et al., 2020), the
266 erosion coefficient (K) is calculated to be $(6.25 \pm 3.13) \times 10^{-6} \text{ m}^{0.1} \text{ yr}^{-1}$ in this area.

267 Because there is no obvious variation in rock erodibility and precipitation in this area
268 (Fig. S2 & S3), we use this value as the erosion coefficient (K) of the Wutai Shan
269 area.

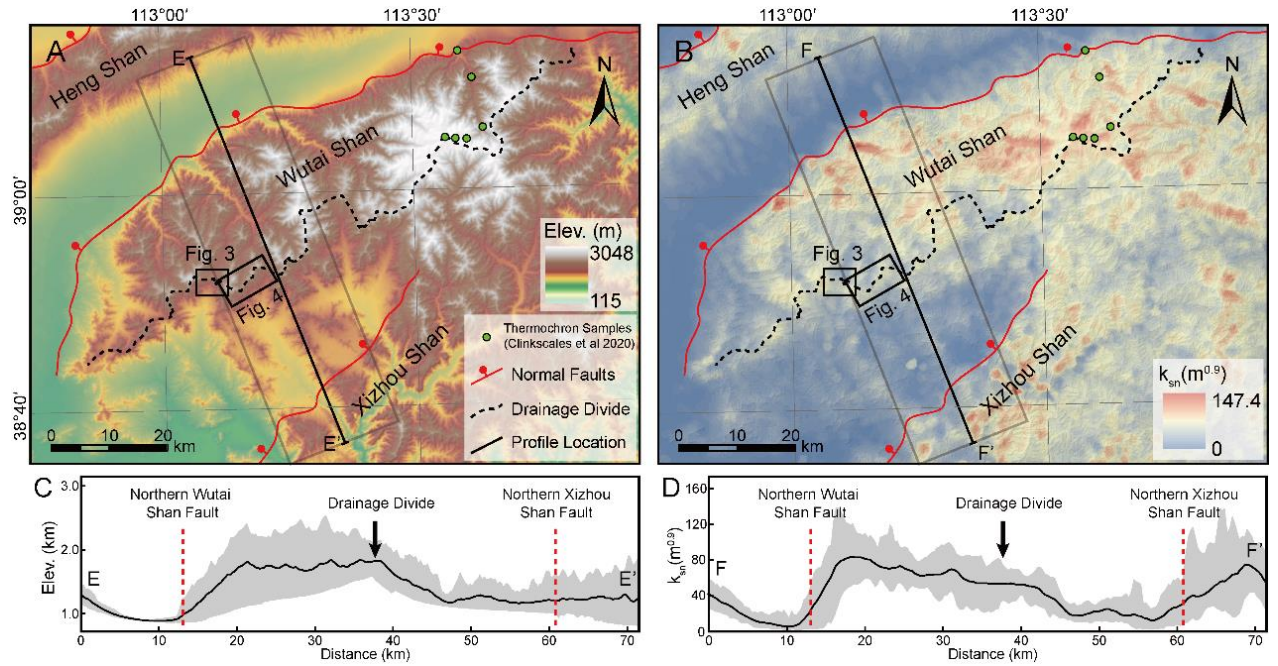
270 We then apply the two new methods to calculate the migration rate of the
271 drainage divide in the Wutai Shan. We first choose three pairs of rivers (Fig. 4A) and
272 acquire their slope-area plots (Figs. 4B, E, H) and the χ -plots (Figs. 4C, F, I).
273 According to the location of the catchment outlets (Fig. 4A), we obtain the outlet
274 elevations (z_b) from the river's long profiles. According to the breaking point of the
275 slope-area regression line (Duvall et al., 2004) (Figs. 4B, E, H), we obtain the values
276 of the critical upstream drainage area (A_{cr}). According to these values, we separate
277 hillslope and channel areas and mark the position of the channel heads on the χ -plots
278 and the topography map (Fig. 4A). For the χ -plots (Figs. 4C, F, I), we obtain the
279 elevations of channel heads (z_{ch}) and χ values based on the coordinate of the channel-
280 head points. According to the location of the channel heads on the river's long
281 profiles, we calculate the slope of the channel heads' tangent lines, and derive the
282 channel-head gradient (S_{ch}). Topographic gradient ($\tan\alpha$ or $\tan\beta$) is calculated through
283 the average slope of the hillslope segment near the channel head (Stokes et al., 2022)
284 (not including the hilltop part).

285 If we assume the rock uplift rate decreases linearly from 0.5 to 0 mm/yr from
286 northwest to southeast of the Wutai Shan horst (~40 km wide), the cross-divide uplift
287 difference in the channel-head points (ΔU_{ch}) (the distance perpendicular to the
288 direction of the boundary fault is ~600 m) is ~0.008 mm/yr. After determining these

289 parameters, we adopt the channel-head-point (Eq. 4) and channel-head-segment (Eq.
290 8) methods, respectively, to calculate the migration rates. The required data for
291 calculation and the migration rates are shown in Table 1. The calculated results for m
292 = 0.35 and 0.55, respectively, are shown in Supplementary Materials (Table S1).

293 The rivers have different characteristics on both sides of the drainage divide, as
294 illustrated on their slope-area plots (Figs. 4B, E, H) and the χ -plots (Figs. 4C, F, I).
295 For the first site (Fig. 4D), the migration rates calculated by the channel-head-point
296 and channel-head-segment methods are 0.21 mm/yr and 0.26 mm/yr, respectively. For
297 the second site (Fig. 4G), the migration rates are 0.23 mm/yr and 0.27 mm/yr,
298 respectively. For the third site (Fig. 4J), 0.21 mm/yr and 0.22 mm/yr, respectively. The
299 drainage divides of all three points are migrating northwestward, which is consistent
300 with the previous result inferred by the cross-divide contrast of slopes in this area
301 (Zhou et al., 2022b). Furthermore, the migration rates calculated by the two methods
302 are comparable in all three sites.

303



304

305 **Figure 2.** Topography (A) and normalized channel steepness (k_{sn}) (B) distribution of
 306 the Wutai Shan horst and surrounding area in the Shanxi Rift System. The black
 307 dashed line shows the location of the main drainage divide. Red lines show the main
 308 active faults. The black lines show the location of profiles E-E' and F-F'. Black
 309 rectangles show the area of Fig. 3B & 4A. Gray boxes show the area of the swath
 310 profiles in Panels C and D. Green dots denote the locations of the low-temperature
 311 thermochronology samples in Clinkscales et al. (2020). The topography data (ALOS
 312 DEM, 12.5 m resolution) is downloaded from the Alaska Satellite Facility (ASF) Data
 313 Search (<https://search.asf.alaska.edu/>). The k_{sn} is calculated using TopoToolbox
 314 (Schwanghart and Scherler, 2014), and the interpolation uses the Kriging method on
 315 ArcGIS. (C) Topography swath profile along E-E'. See location in Panel A. (D) k_{sn}
 316 swath profile along F-F'. See location in Panel B. The swath profiles are extracted
 317 using TopoToolbox (Schwanghart and Scherler, 2014). The red dashed lines show the
 318 location of the main active normal faults, and the black arrow shows the location of

319 the main drainage divide. Both swath profiles are 20 km wide (10 km on each side).

320

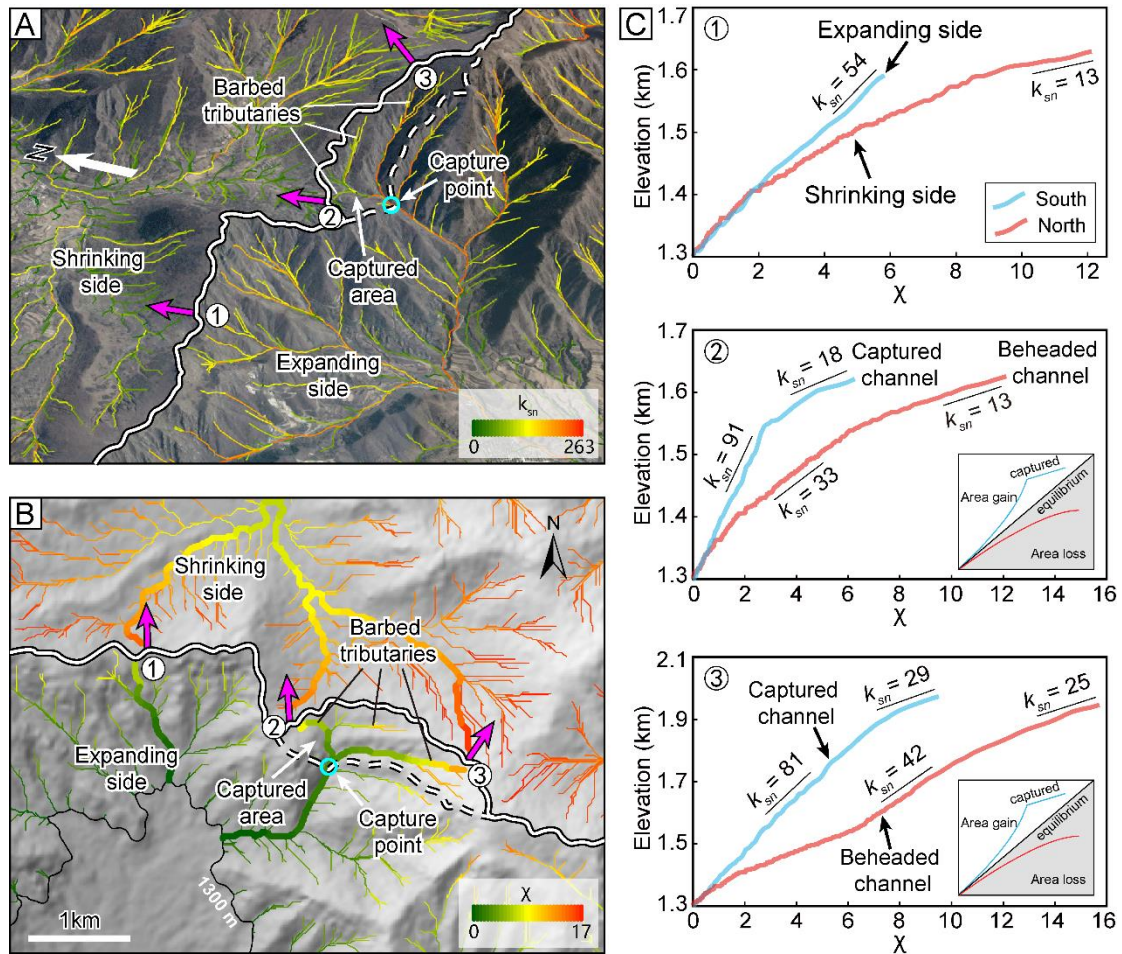
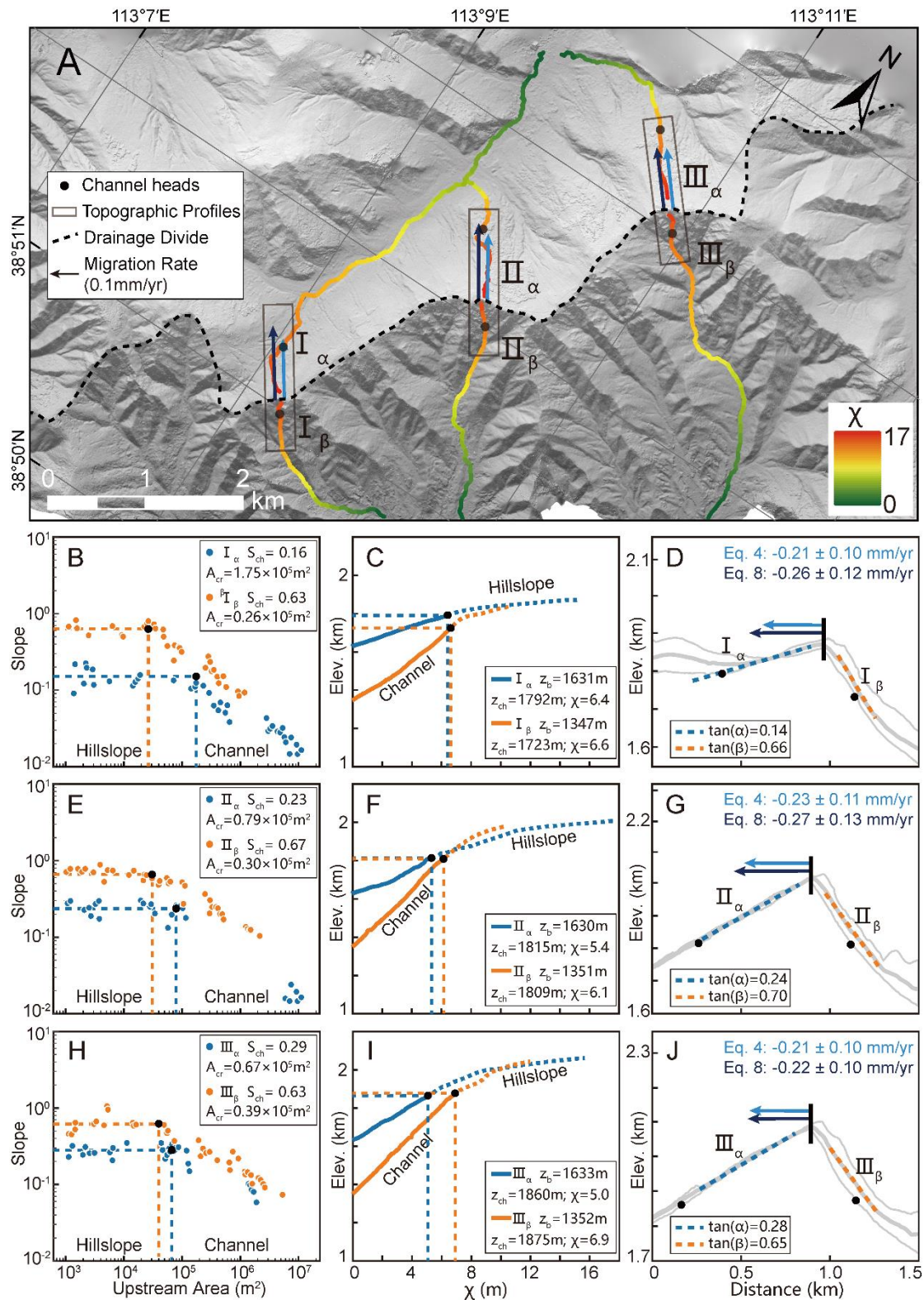


Figure 3. Perspective views and χ map of the drainage divide in the Wutai Shan (see Fig. 2 for location). (A) Perspective views of a captured area and the channels mapped with k_{sn} . The south side of the drainage divide has steeper channels and higher k_{sn} than the north side. Magenta arrows show drainage divide migration directions. The satellite image is from Google Earth. (B) χ map of this area with the outlet elevation of 1300 m. The south side of the drainage divide has lower χ values than the north side. It should be noted that the catchment outlet at the north side of the drainage basins (the 1300 m contour) is out of the map. The χ -plots of the rivers in bold lines are shown in Panel C. The topography data (ALOS DEM, 12.5 m resolution) is

331 downloaded from the Alaska Satellite Facility (ASF) Data Search
332 (<https://search.asf.alaska.edu/>). (C) χ -plots of the three paired rivers in Panel B. The blue
333 and red curves correspond to the rivers on the south and north sides, respectively. The
334 χ -plot of River 1 is steeper on the south side, indicating that the river on the south side
335 is expanding and the river on the north side is shrinking. The χ -plots of Rivers 2 and 3
336 in the captured area show obvious characteristics of the captured and beheaded rivers.
337 The χ -plot is extracted using TAK (Forte and Whipple, 2019) and TopoToolbox
338 (Schwanghart and Scherler, 2014).
339



340

341 **Figure 4.** Analytical results of the Wutai Shan drainage divide. (A) High-resolution

342 hill-shade map (0.67 m spatial resolution) of the Wutai Shan. The black dashed line

343 shows the location of the main drainage divide. Colored lines show the three pairs of

344 selected channels used for analysis. The black dots are the channel heads. Black
345 rectangles show the location of the cross-divide topography swath profiles. The black
346 arrows show the direction of drainage-divide migration (**B, E, H**) Slope-area plots of
347 the three pairs of selected channels. The blue and orange dots are the slope-area plots
348 of the north (α) and south (β) sides of the drainage divide respectively. The black dots
349 represent the channel heads. (**C, F, I**) χ -plots of the selected channels. The blue and
350 orange lines are the χ -plots of the north (α) and south (β) sides of the drainage divide
351 respectively. The black dots represent the channel heads. (**D, G, J**) Cross-divide
352 topography swath profiles with the drainage-divide migration rates. The locations of
353 the profiles are in Panel A. The light and dark blue arrows are the drainage-divide
354 migration rates calculated by the channel-head-point (Eq. 4) and channel-head-
355 segment (Eq. 8) methods respectively.

356

357 **3.2 Yingwang Shan**

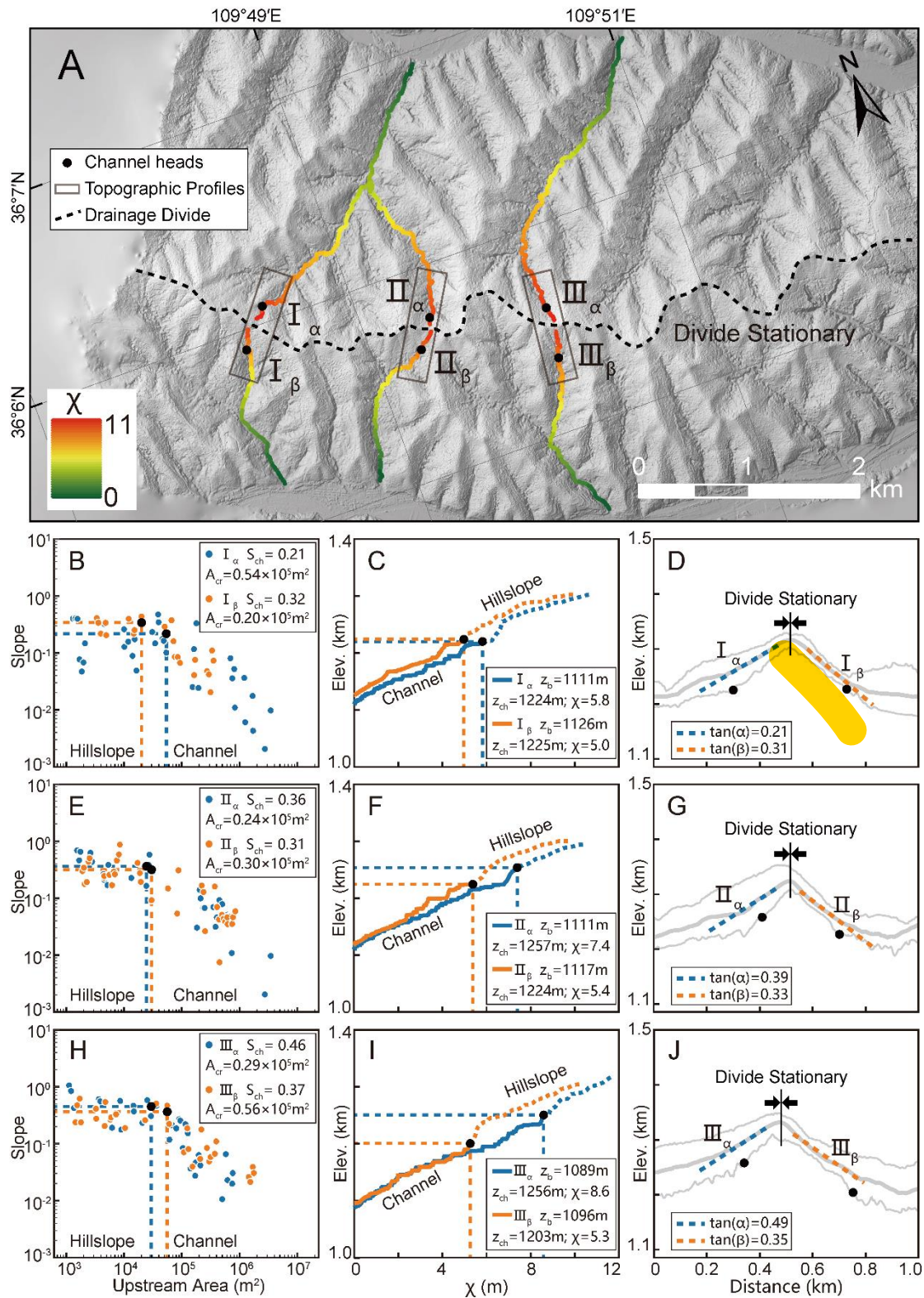
358 The Loess Plateau is hosted by the tectonically stable Ordos Block of the North
359 China craton (Yin, 2010; Su et al., 2021). Over the past 2.6 million years, it has
360 accumulated tens to hundreds of meters of eolian sediments (Yan et al., 2014),
361 draping preexisting topography (Xiong et al., 2014). There is no active fault and little
362 to no variation in rock erodibility and precipitation within the area (Shi et al., 2020;
363 Zhou et al., 2022b).

364 We apply the two methods to Yingwang Shan of Loess Plateau to calculate the

365 drainage-divide migration rate. Similar to the Wutai Shan site, we obtain the slope-
366 area plots (Figs. 5 B, E, H), the χ -plots (Figs. 5 C, F, I), and extract the values of A_{cr} ,
367 S_{ch} , z_b , z_{ch} , χ , $\tan\alpha$ and $\tan\beta$ of the rivers. The rate of soil erosion in the study area is
368 about $500 \text{ t}\cdot\text{km}^{-2}\cdot\text{yr}^{-1}$ according to the distribution of silt discharge (Fu, 1989).
369 Combining with the assumption of the density of loess, $1.65 \text{ t}\cdot\text{m}^{-3}$, the present-day
370 erosion rate in the study area is calculated to be $0.3 \text{ mm}\cdot\text{yr}^{-1}$. Because there is no
371 obvious unequal uplift in this region, we assign that ΔU_{ch} is zero. We also assume $n =$
372 1 and $m = 0.45$ in the calculation (Wobus et al., 2006; DiBiase et al., 2010; Perron and
373 Royden, 2012; Wang et al., 2021). Then, we use the methods of channel-head
374 parameters (Eq. 7) and channel segments (Eq. 11) to calculate the drainage-divide
375 migration rates. The required data for calculation and the migration rates are shown in
376 Table 1.

377 All results of the three points show that the drainage-divide migration rate here is
378 close to zero, no matter which method is used in the calculation. The results show that
379 the drainage divide of the study site is in topographical equilibrium, which is
380 consistent with the inference in previous studies (Willett et al., 2014, Zhou et al.,
381 2022b).

382



383

384 **Figure 5.** Analytical results of the Yingwang Shan in the Loess Plateau. (A) High-
 385 resolution hill-shade map (0.84 m spatial resolution). The black dotted line shows the
 386 location of the main drainage divide. Colored lines show the three pairs of selected

387 channels used for analysis. The black dots represent the channel heads. Black
388 rectangles show the location of the cross-divide topography swath profiles. **(B, E, H)**
389 Slope-area plots of the three pairs of selected channels. The blue and orange dots are
390 the data of the north (α) and south (β) sides of the drainage divide respectively. The
391 black dots represent the channel heads. **(C, F, I)** χ -plots of the selected channels. The
392 blue and orange lines are the χ -plots of the north (α) and south (β) sides of the
393 drainage divide respectively. The black dots represent the channel heads. **(D, G, J)**
394 The cross-divide topography swath profiles. The locations of the swath profiles are in
395 Panel A.
396

Table 1. Channel parameters and migration rates of drainage divides in two field cases.

Natural Cases	No.	A_{cr} ($\times 10^5 \text{m}^2$)	S_{ch}	z_b (m)	z_{ch} (m)	χ	$\tan\alpha$	$\tan\beta$	ΔU_{ch} (mm/yr)	D_{mr} (mm/yr) (Channel-head-point method)	D_{mr} (mm/yr) (Channel-head-segment method)
Wutai Shan	Fig. 4 I α	1.75	0.16	1631	1792	6.4	0.14	0.66	~ 0.008	-0.21 ± 0.10	-0.26 ± 0.12
	Fig. 4 I β	0.26	0.63	1347	1723	6.6					
	Fig. 4 II α	0.79	0.23	1630	1815	5.4	0.24	0.70	~ 0.008	-0.23 ± 0.11	-0.27 ± 0.13
	Fig. 4 II β	0.30	0.67	1351	1809	6.1					
	Fig. 4 III α	0.67	0.29	1633	1860	5.0	0.28	0.65	~ 0.008	-0.21 ± 0.10	-0.22 ± 0.10
Fig. 4 III β	0.39	0.63	1352	1875	6.9						
Yingwang Shan	Fig. 5 I α	0.54	0.21	1111	1224	5.8	0.21	0.31	0	~ 0.03	~ -0.01
	Fig. 5 I β	0.20	0.32	1126	1225	5.0					
	Fig. 5 II α	0.24	0.36	1111	1257	7.4	0.39	0.33	0	~ 0.02	~ -0.01
	Fig. 5 II β	0.30	0.31	1117	1224	5.4					
	Fig. 5 III α	0.29	0.46	1089	1256	8.6	0.49	0.35	0	~ 0.02	~ -0.01
Fig. 5 III β	0.56	0.37	1096	1203	5.3						

399 **4. Discussion**

400 **4.1 Location of channel heads**

401 Willett et al. (2014) pioneered the use of cross-divide χ contrast to gauge the
402 horizontal motion of drainage divides. According to their method, drainage divides
403 are predicted to move toward the side with a higher χ value to achieve geomorphic
404 equilibrium. However, in a region with spatially variable uplift rates, lithology, or
405 precipitation, χ contrast may fail to reflect the drainage-divide migration (Willett et
406 al., 2014; Whipple et al., 2017; Forte and Whipple, 2018; Wu et al., 2022; Zhou and
407 Tan, 2023). In a tectonically active area, the cross-divide χ contrast can only be used
408 in a small area where rock type, precipitation, and uplift rate are nearly uniform
409 (Willett et al., 2014). Combining the advantages of the χ and Gilbert metrics methods,
410 Zhou et al. (2022a) proposed to use the χ contrast with a high base level to calculate
411 the k_{sn} values at the channel heads on both sides of a drainage divide, and quantified
412 the migration rate of drainage divides at the eastern margin of Tibet.

413 To reduce the cross-divide difference in uplift rate, precipitation, and rock
414 strength, the Gilbert metrics or χ -comparison method in Zhou et al. (2022a) should
415 compare the parameters of points (slope, relief, elevation, and k_{sn}) on both sides of the
416 divide as closely as possible. As the hillslope area (above the channel head) does not
417 follow Eq. 1 (Stoke and Dietrich, 2006; Stark, 2010; Braun et al., 2018; Dahlquist et
418 al., 2018), the channel heads are the closest point to the divide, following Eq. 1.
419 Channel heads, therefore, are suitable for measuring the drainage-divide stability with

420 parameters of the upstream drainage area and channel gradient (Forte and Whipple,
421 2018; Zhou et al., 2022a). However, limited by the resolution of DEM, the location of
422 the channel heads cannot always be accurately identified. The channel head
423 parameters for calculating the migration rates are usually based on empirical values in
424 previous studies (e.g., $A_{cr} = 10^5 \text{ m}^2$ in Zhou et al. (2022a)), which may induce
425 uncertainties.

426 In this study, we advocate the use of high-resolution DEM to determine a more
427 accurate position and related parameters of the channel head. The use of UAVs to
428 obtain the local DEM has become highly efficient. We advance the theory to calculate
429 the drainage-divide migration rate based on the measured channel-head parameters.
430 With the help of the aerial photography of UAVs and the SfM techniques, it is
431 possible to obtain the high-resolution topography data of drainage divides (Figs. 4A &
432 5A) and get the required parameters (including the exact locations of the channel
433 heads across the drainage divide) through topography analysis, which could improve
434 the quantitative research on the drainage-divide migration. Furthermore, the method
435 provides a new avenue to combine with catchment-wide ^{10}Be erosion rate or low-
436 temperature thermochronology data to calculate the migration rate, which has great
437 potential for application in places where some variables are hard to be constrained.

438

439 **4.2 Cross-divide difference in the uplift rate of the channel heads**

440 Although the channel heads across the divide are very close on the spatial scale of

441 an orogenic belt, differential uplift between the channel heads (ΔU_{ch}) could still exist,
442 especially in a tilting horst, such as the Wutai Shan. The cross-divide difference in
443 uplift rate could impact the calculation of the migration rate of drainage divides (Zhou
444 et al., 2022a).

445 In this study, we quantify the influence of the cross-divide difference in rock
446 uplift rate (ΔU_{ch}) on the calculation of the migration rate of drainage divides at the
447 Wutai Shan, benefiting from the available tectonic and chronological research
448 (Clinkscales et al., 2020) and the newly obtained high-resolution topographic data. In
449 the Wutai Shan horst, ΔU_{ch} across the drainage divide is ~ 0.008 mm/yr. We estimate
450 the influence of ΔU_{ch} on the drainage-divide migration rate in this case study, which
451 can reduce the error theoretically. If ΔU_{ch} is ignored, the drainage-divide migration
452 rate would decrease by $\sim 4\%$ in the Wutai Shan case. Although $\sim 4\%$ seems to be
453 negligible, such a ratio will increase if the mountain belt is narrower, the tilting uplift
454 is stronger, or the divide is closer to the steady state (i.e., the migration rate is lower)
455 (Whipple et al., 2017; Ye et al., 2022). In other words, the differential uplift may play
456 a significant influence on the measurement of drainage-divide stability in some
457 situations. If we consider an extreme example where the main drainage divide of a
458 tilting mountain range (relatively narrow in width) is at a steady state, the gradient,
459 relief, and elevation of the channel heads (collectively called “Gilbert metrics”) (Forte
460 and Whipple, 2018) will show a systematic cross-divide difference in theory. In this
461 case, the drainage divide would be considered unstable if ΔU_{ch} were neglected.
462 Therefore, this study highlights that ΔU_{ch} should be taken into account, either in a

463 qualitative or a quantitative evaluation of the stability of drainage divides using the
464 parameters on the channel heads.

465

466 **4.3 Limitations and uncertainties**

467 This study develops the method to calculate the drainage-divide migration rate
468 based on the measured channel-head parameters. However, uncertainties still exist
469 because of the limitations of this technique. First, we assume the erosion coefficient
470 (K) is the same on both sides of a drainage divide in the derivation of the equations. If
471 there are differences in rock erodibility or precipitation across the divide, uncertainties
472 should exist in the results. Second, the calculation of migration rate is based on the
473 erosion rates at the channel area in this study. However, the occurrence of drainage-
474 divide migration is directly driven by the differential erosion of the hillslope area
475 across the divide, mainly via the processes including landslide, collapse, and diffusion
476 (Stoke and Dietrich, 2006; Stark, 2010; Braun et al., 2018; Dahlquist et al., 2018).

477 Such discontinuous processes in the hillslope area make it challenging to constrain
478 erosion rates over such short timescales. Over a relatively longer period (i.e., spanning
479 multiple seismic and climatic cycles), the erosion rate at the channel head area in this
480 study can be comparable with that at the hillslope area (Hurst et al., 2012; Godard et
481 al., 2020).

482 The accuracy of the data and parameters can also impact the reliability of the
483 results. First, we use the typical values of $n = 1$ and $m/n = 0.45$ in the two natural
484 cases to calculate the migration rate. If the actual values largely deviate from the

485 assumption, errors would be introduced into the results. For this reason, we have
486 added the cases of $m/n = 0.35$ and 0.55 in Supplementary Materials. Further
487 estimation of these values (Mudd et al., 2018) could improve the accuracy of the
488 results. Second, in the case of the Wutai Shan, we refer to the geological and low-
489 temperature thermochronology studies and assume a 0.50 ± 0.25 mm/yr erosion rate at
490 the northern margin of the Wutai Shan (i.e., the footwall of the North Wutai Shan
491 fault). Combining with the present-day k_{sn} , we calculate the erosion coefficient (K)
492 and derive the migration rates of the drainage divide. If the present-day erosion rate
493 deviates from the assumption, errors would be inevitable in the results. Moreover, the
494 horizontal and vertical errors of the DEM data, as well as the calculation errors in
495 slope, upstream area and channel steepness can also affect the reliability of the results.
496 In the case study of the Yingwang Shan, the lush vegetation may bring errors to the
497 DEM data based on the SfM technology. The application of airborne light detection
498 and ranging (LiDAR) technology may help reduce this error. Future studies should
499 take these challenges into account and overcome them.

500

501 **5. Conclusions**

502 We have developed a new method (called the "channel-head-point method") to
503 calculate the migration rate of drainage divides based on channel-head parameters. We
504 have also improved the previously proposed "channel-head-segment method" (Zhou
505 et al., 2022a) to adapt the theory to areas where the parameters of channel-heads can

506 be accurately determined.

507 Using the new methods and high-resolution topographic data, we determined the
508 exact locations of the channel heads on both sides of the drainage divide and
509 quantified the drainage-divide migration rates in two natural cases in North China:
510 Wutai Shan in the Shanxi Rift, and Yingwang Shan in the Loess Plateau. The
511 migration rates of the study sites in the Wutai Shan are 0.21-0.27 mm/yr
512 (northwestward). The rates are close to zero in the Yingwang Shan.

513 Based on the locations of the channel heads and the uplift gradient of the Wutai
514 Shan, we calculated the cross-divide difference in the uplift rate at the channel heads
515 (ΔU_{ch}), which is taken into account in the calculation of the drainage-divide migration
516 rate for the first time. If ΔU_{ch} is overlooked, the drainage-divide migration rate of the
517 study sites in the Wutai Shan will be underestimated by ~4%. Our study highlights
518 that ΔU_{ch} should be considered in the assessment of drainage divide stability based on
519 the cross-divide difference in channel-head parameters.

520

521 **Data availability.** The analysis of data is based on the Matlab toolbox TAK (Forte
522 and Whipple, 2019) and TopoToolbox (Schwanghart and Scherler, 2014). The
523 topography data (ALOS DEM, 12.5 m resolution) is downloaded from the Alaska
524 Satellite Facility (ASF) Data Search (<https://search.asf.alaska.edu/>).

525 **Acknowledgements.** We would like to thank the Editor Simon Mudd, the
526 Reviewer Thomas Bernard, and an anonymous reviewer whose suggestions have
527 greatly improved the paper.

528 **Financial support.** This study is supported by the CAS Pioneer Hundred Talents
529 Program (E2K2010010) and the Fundamental Research Funds for the State Key
530 Laboratory of Earthquake Dynamics (LED2021A02).

531 **Competing interests.** The authors declare that they have no conflict of interest.

532 **Author contributions.** XT and CZ contributed to the design of the research
533 scheme. CZ performed the geomorphic analyses. CZ, XT, and FS carried out field
534 data collection. CZ, XT, YL, and FS contributed to the text and reviewed the paper.

535

536 **References**

537 Authemayou, C., Brocard, G., Delcaillau, B., Molliex, S., Pedoja, K., Husson, L., et
538 al., 2018. Unraveling the roles of asymmetric uplift, normal faulting and
539 groundwater flow to drainage rearrangement in an emerging karstic landscape.
540 Earth Surface Processes and Landforms, 43(9), 1885-1898.

541 <https://doi.org/10.1002/esp.4363>

542 Beeson, H.W., McCoy, S.W., Keen-Zebert, A., 2017. Geometric disequilibrium of
543 river basins produces long-lived transient landscapes. Earth Planet Sc Lett 475,
544 34-43. <https://doi.org/10.1016/j.epsl.2017.07.010>

545 Bernard, T., Sinclair, H.D., Gailleton, B., Fox, M., 2021. Formation of Longitudinal
546 River Valleys and the Fixing of Drainage Divides in Response to Exhumation of
547 Crystalline Basement. Geophys Res Lett 48.

548 <https://doi.org/10.1029/2020gl092210>.

549 Bian, S., Tan, X., Liu, Y., Fan, S., Gong, J., Zhou, C., Shi, F., Murphy, M.A., 2024.
550 Orographic rainfall drives the Himalaya drainage divide to move north.
551 Geomorphology, 108952. <https://doi.org/10.1016/j.geomorph.2023.108952>

552 Bonnet, S., 2009. Shrinking and splitting of drainage basins in orogenic landscapes
553 from the migration of the main drainage divide. Nature Geoscience 2, 766-771.
554 <https://doi.org/10.1038/ngeo666>

555 Bookhagen, B., Strecker, M.R., 2012. Spatiotemporal trends in erosion rates across a
556 pronounced rainfall gradient: Examples from the southern Central Andes. Earth
557 Planet Sc Lett 327-328, 97-110. <https://doi.org/10.1016/j.epsl.2012.02.005>

558 Braun, J., 2018. A review of numerical modeling studies of passive margin
559 escarpments leading to a new analytical expression for the rate of escarpment
560 migration velocity. Gondwana Research 53, 209-224.
561 <https://doi.org/10.1016/j.gr.2017.04.012>

562 Burbank, D.W., Leland, J., Fielding, E., Anderson, R.S., Brozovic, N., Reid, M.R.,
563 Duncan, C., 1996. Bedrock incision, rock uplift and threshold hillslopes in the
564 northwestern Himalayas. Nature 379, 505–510. <https://doi.org/10.1038/379505a0>

565 Burbank, D.W., Anderson, R.S., 2001. Tectonic Geomorphology. Blackwell Science,
566 Massachusetts p. 274.

567 Chen, C.-Y., Willett, S.D., Christl, M., Shyu, J.B.H., 2021. Drainage basin dynamics
568 during the transition from early to mature orogeny in Southern Taiwan. Earth
569 Planet Sc Lett 562. <https://doi.org/10.1016/j.epsl.2021.116874>

570 Clark, M.K., Schoenbohm, L.M., Royden, L.H., Whipple, K.X., Burchfiel, B.C.,

571 Zhang, X., Tang, W., Wang, E., Chen, L., 2004. Surface uplift, tectonics, and
572 erosion of eastern Tibet from large-scale drainage patterns. *Tectonics* 23, 1-20.
573 <https://doi.org/10.1029/2002tc001402>

574 Clift, P.D., Blusztajn, J., 2005. Reorganization of the western Himalayan river system
575 after five million years ago. *Nature* 438, 1001-1003.
576 <https://doi.org/10.1038/nature04379>

577 Clinkscales, C., Kapp, P., Wang, H., 2020. Exhumation history of the north-central
578 Shanxi Rift, North China, revealed by low-temperature thermochronology. *Earth
579 Planet Sc Lett* 536, 116146. <https://doi.org/10.1016/j.epsl.2020.116146>

580 Clubb, F.J., Mudd, S.M., Milodowski, D.T., Hurst, M.D., Slater, L.J., 2014. Objective
581 extraction of channel heads from high-resolution topographic data. *Water
582 Resources Research* 50, 4283-4304. <https://doi.org/10.1002/2013wr015167>

583 Crosby, B.T., Whipple, K.X., 2006. Knickpoint initiation and distribution within
584 fluvial networks: 236 waterfalls in the Waipaoa River, North Island, New
585 Zealand. *Geomorphology* 82, 16-38.
586 <https://doi.org/10.1016/j.geomorph.2005.08.023>

587 Dahlquist, M.P., West, A.J., Li, G., 2018. Landslide-driven drainage divide migration.
588 *Geology* 46, 403-406. <https://doi.org/10.1130/g39916.1>

589 Deng, B., Chew, D., Mark, C., Liu, S., Cogné, N., Jiang, L., O'Sullivan, G., Li, Z., Li,
590 J., 2020. Late Cenozoic drainage reorganization of the paleo-Yangtze river
591 constrained by multi-proxy provenance analysis of the Paleo-lake Xigeda. *GSA
592 Bulletin*. <https://doi.org/10.1130/b35579.1>

593 DiBiase, R.A., Whipple, K.X., Heimsath, A.M., Ouimet, W.B., 2010. Landscape form
594 and millennial erosion rates in the San Gabriel Mountains, CA. Earth Planet Sc
595 Lett 289, 134-144. <https://doi.org/10.1016/j.epsl.2009.10.036>

596 Duvall, A., 2004. Tectonic and lithologic controls on bedrock channel profiles and
597 processes in coastal California. J Geophys Res 109.
598 <https://doi.org/10.1029/2003jf000086>

599 Forte, A.M., Whipple, K.X., 2018. Criteria and tools for determining drainage divide
600 stability. Earth Planet Sc Lett 493, 102–117.
601 <https://doi.org/10.1016/j.epsl.2018.04.026>

602 Forte, A.M., Whipple, K.X., 2019. Short communication: The Topographic Analysis
603 Kit (TAK) for TopoToolbox. Earth Surface Dynamics 7, 87–95.
604 <https://doi.org/10.5194/esurf-7-87-2019>

605 Forte, A.M., Yanites, B.J., Whipple, K.X., 2016. Complexities of landscape evolution
606 during incision through layered stratigraphy with contrasts in rock strength.
607 Earth Surface Processes and Landforms 41, 1736-1757.
608 <https://doi.org/10.1002/esp.3947>

609 Fu, B., 1989. Soil erosion and its control in the loess plateau of China. Soil Use and
610 Management 5, 76-82. <https://doi.org/10.1111/j.1475-2743.1989.tb00765.x>

611 Gallen, S.F., 2018. Lithologic controls on landscape dynamics and aquatic species
612 evolution in post-orogenic mountains. Earth Planet Sc Lett 493, 150-160.
613 <https://doi.org/10.1016/j.epsl.2018.04.029>

614 Godard, V., Dosseto, A., Fleury, J., Bellier, O., Siame, L., 2019. Transient landscape

615 dynamics across the Southeastern Australian Escarpment. Earth Planet Sc Lett
616 506, 397-406. <https://doi.org/10.1016/j.epsl.2018.11.017>

617 Godard, V., Hippolyte, J.-C., Cushing, E., Espurt, N., Fleury, J., Bellier, O., Ollivier,
618 V., 2020. Hillslope denudation and morphologic response to a rock uplift
619 gradient. Earth Surface Dynamics 8, 221-243. [https://doi.org/10.5194/esurf-8-](https://doi.org/10.5194/esurf-8-221-2020)
620 [221-2020](https://doi.org/10.5194/esurf-8-221-2020)

621 Goren, L., Fox, M., Willett, S.D., 2014. Tectonics from fluvial topography using
622 formal linear inversion: Theory and applications to the Inyo Mountains,
623 California. Journal of Geophysical Research: Earth Surface 119, 1651-1681.
624 <https://doi.org/10.1002/2014jf003079>

625 Hancock, G.S., Anderson, R.S., 2002. Numerical modeling of fluvial strath-terrace
626 formation in response to oscillating climate. GSA Bulletin 114, 1131-1142.
627 [https://doi.org/10.1130/0016-7606\(2002\)114<1131:nmofst>2.0.co;2](https://doi.org/10.1130/0016-7606(2002)114<1131:nmofst>2.0.co;2)

628 He, C., Yang, C.J., Turowski, J.M., Rao, G., Roda-Boluda, D.C., Yuan, X.P., 2021.
629 Constraining tectonic uplift and advection from the main drainage divide of a
630 mountain belt. Nat Commun 12, 544. [https://doi.org/10.1038/s41467-020-20748-](https://doi.org/10.1038/s41467-020-20748-2)
631 [2](https://doi.org/10.1038/s41467-020-20748-2)

632 Hilley, G.E., Arrowsmith, J.R., 2008. Geomorphic response to uplift along the
633 Dragon's Back pressure ridge, Carrizo Plain, California. Geology 36.
634 <https://doi.org/10.1130/g24517a.1>

635 Hoorn, C., Wesselingh, F.P., Steege, H.T., Bermudez, M.A., Antonelli, A., 2010.
636 Amazonia Through Time: Andean Uplift, Climate Change, Landscape Evolution,

637 and Biodiversity. *Science* 330, 927-931. <https://doi.org/10.1126/science.1194585>

638 Hoskins, A.M., Attal, M., Mudd, S.M., Castillo, M., 2023. Topographic Response to
639 Horizontal Advection in Normal Fault-Bound Mountain Ranges. *Journal of*
640 *Geophysical Research: Earth Surface* 128. <https://doi.org/10.1029/2023jf007126>.

641 Howard, A.D., Dietrich, W.E., Seidl, M.A., 1994. Modeling fluvial erosion on
642 regional to continental scales. *Journal of Geophysical Research: Solid Earth* 99,
643 13971-13986. <https://doi.org/10.1029/94jb00744>

644 Howard, A.D., Kerby, G., 1983. Channel changes in badlands. *Geological Society of*
645 *America Bulletin* 94, 739. [https://doi.org/10.1130/0016-](https://doi.org/10.1130/0016-7606(1983)94<739:CCIB>2.0.CO;2)
646 [7606\(1983\)94<739:CCIB>2.0.CO;2](https://doi.org/10.1130/0016-7606(1983)94<739:CCIB>2.0.CO;2)

647 Hu, K., Fang, X., Ferrier, K.L., Granger, D.E., Zhao, Z., Ruetenik, G.A., 2021.
648 Covariation of cross-divide differences in denudation rate and χ : Implications for
649 drainage basin reorganization in the Qilian Shan, northeast Tibet. *Earth Planet Sc*
650 *Lett* 562, 116812. <https://doi.org/10.1016/j.epsl.2021.116812>

651 Hurst, M.D., Mudd, S.M., Walcott, R., Attal, M., Yoo, K., 2012. Using hilltop
652 curvature to derive the spatial distribution of erosion rates. *Journal of*
653 *Geophysical Research: Earth Surface* 117, n/a-n/a.
654 <https://doi.org/10.1029/2011jf002057>

655 Jiao, R., Fox, M., Yang, R., 2022. Late Cenozoic erosion pattern of the eastern margin
656 of the Sichuan Basin: Implications for the drainage evolution of the Yangtze
657 River. *Geomorphology* 398, 108025.
658 <https://doi.org/10.1016/j.geomorph.2021.108025>

659 Kirby, E., Whipple, K., 2001. Quantifying differential rock-uplift rates via stream
660 profile analysis. *Geology* 29, 415-418. [https://doi.org/10.1130/0091-
661 7613\(2001\)029<0415:Qdrurv>2.0.Co;2](https://doi.org/10.1130/0091-7613(2001)029<0415:Qdrurv>2.0.Co;2)

662 Kirby, E., Whipple, K., Tang, W., Chen, Z., 2003. Distribution of active rock uplift
663 along the eastern margin of the Tibetan Plateau: Inferences from bedrock channel
664 longitudinal profiles. *Journal of Geophysical Research*, 108(B4), 2217,
665 <https://doi.org/10.1029/2001JB000861>.

666 Kirby, E., Whipple, K.X., 2012. Expression of active tectonics in erosional
667 landscapes. *J Struct Geol* 44, 54-75. <https://doi.org/10.1016/j.jsg.2012.07.009>

668 Kirkpatrick, H.M., Moon, S., Yin, A., Harrison, T.M., 2020. Impact of fault damage
669 on eastern Tibet topography. *Geology* 48. <https://doi.org/10.1130/g48179.1>

670 Ma, Z., Zhang, H., Wang, Y., Tao, Y., Li, X., 2020. Inversion of Dadu River Bedrock
671 Channels for the Late Cenozoic Uplift History of the Eastern Tibetan Plateau.
672 *Geophys Res Lett* 47. <https://doi.org/10.1029/2019gl086882>

673 Mandal, S.K., Lupker, M., Burg, J.-P., Valla, P.G., Haghypour, N., Christl, M., 2015.
674 Spatial variability of ¹⁰Be-derived erosion rates across the southern Peninsular
675 Indian escarpment: A key to landscape evolution across passive margins. *Earth
676 Planet Sc Lett* 425, 154-167. <https://doi.org/10.1016/j.epsl.2015.05.050>

677 Molnar, P., England, P., 1990. Late Cenozoic uplift of mountain ranges and global
678 climate change: chicken or egg? *Nature* 346, 29-34.
679 https://doi.org/10.1038_346029a0

680 Mudd, S.M., Clubb, F.J., Gailleton, B., Hurst, M.D., 2018. How concave are river

681 channels? Earth Surface Dynamics 6, 505-523. <https://doi.org/10.5194/esurf-6->
682 [505-2018](https://doi.org/10.5194/esurf-6-505-2018)

683 Musher, L.J., Giakoumis, M., Albert, J., Rio, G.D., Rego, M., Thom, G., Aleixo, A.,
684 Ribas, C.C., Brumfield, R.T., Smith, B.T., 2021. River network rearrangements
685 promote speciation in lowland Amazonian birds. Cold Spring Harbor Laboratory.
686 <https://doi.org/10.1126/sciadv.abn1099>

687 Perron, J.T., Dietrich, W.E., Kirchner, J.W., 2008. Controls on the spacing of first-
688 order valleys. J Geophys Res 113. <https://doi.org/10.1029/2007jf000977>

689 Perron, J.T., Royden, L., 2012. An integral approach to bedrock river profile analysis.
690 Earth Surface Processes and Landforms 38, 570-576.
691 <https://doi.org/10.1002/esp.3302>

692 Pritchard, D., Roberts, G.G., White, N.J., Richardson, C.N., 2009. Uplift histories
693 from river profiles. Geophys Res Lett 36. <https://doi.org/10.1029/2009gl040928>

694 Royden, L., Clark, M., Whipple, K., 2000. Evolution of river elevation profiles by
695 bedrock incision: Analytical solutions for transient river profiles related to
696 changing uplift and precipitation rates. Eos Trans. AGU 81.

697 Safran, E.B., Bierman, P.R., Aalto, R., Dunne, T., Whipple, K.X., Caffee, M., 2005.
698 Erosion rates driven by channel network incision in the Bolivian Andes. Earth
699 Surface Processes and Landforms 30, 1007-1024.
700 <https://doi.org/10.1002/esp.1259>

701 Sassolas-Serrayet, T., Cattin, R., Ferry, M., Godard, V., Simoes, M., 2019. Estimating
702 the disequilibrium in denudation rates due to divide migration at the scale of

703 river basins. *Earth Surface Dynamics* 7, 1041-1057.
704 <https://doi.org/10.5194/esurf-7-1041-2019>

705 Scheingross, J.S., Limaye, A.B., McCoy, S.W., Whittaker, A.C., 2020. The shaping of
706 erosional landscapes by internal dynamics. *Nature Reviews Earth &*
707 *Environment* 1, 661-676. <https://doi.org/10.1038/s43017-020-0096-0>

708 Scherler, D., Schwanghart, W., 2020. Drainage divide networks – Part 2: Response to
709 perturbations. *Earth Surface Dynamics* 8, 261-274. [https://doi.org/10.5194/esurf-](https://doi.org/10.5194/esurf-8-261-2020)
710 [8-261-2020](https://doi.org/10.5194/esurf-8-261-2020)

711 Schildgen, T.F., van der Beek, P.A., D'Arcy, M., Roda-Boluda, D., Orr, E.N.,
712 Wittmann, H., 2022. Quantifying drainage-divide migration from orographic
713 rainfall over geologic timescales: Sierra de Aconquija, southern Central Andes.
714 *Earth Planet Sc Lett* 579, 117345. <https://doi.org/10.1016/j.epsl.2021.117345>

715 Schlunegger, F., Norton, K.P., Zeilinger, G., 2011. Climatic Forcing on Channel
716 Profiles in the Eastern Cordillera of the Coroico Region, Bolivia. *The Journal of*
717 *Geology* 119, 97-107. <https://doi.org/10.1086/657407>

718 Schwanghart, W., D., S., 2014. Short Communication: TopoToolbox 2 – MATLAB-
719 based software for topographic analysis and modeling in Earth surface sciences.
720 *Earth Surface Dynamics* 2, 1-7. <https://doi.org/10.5194/esurf-2-1-2014>

721 Shelef, E., Goren, L., 2021. The rate and extent of wind-gap migration regulated by
722 tributary confluences and avulsions. *Earth Surface Dynamics*, 9(4), 687-700.
723 <https://doi.org/10.5194/esurf-9-687-2021>

724 Shi, F., Tan, X., Zhou, C., Liu, Y., 2021. Impact of asymmetric uplift on mountain

725 asymmetry: Analytical solution, numerical modeling, and natural examples.
726 Geomorphology 389, 107862. <https://doi.org/10.1016/j.geomorph.2021.107862>

727 Shi, W., Dong, S., Hu, J., 2020. Neotectonics around the Ordos Block, North China: A
728 review and new insights. Earth-Science Reviews 200, 102969.
729 <https://doi.org/10.1016/j.earscirev.2019.102969>

730 Stark, C.P., 2010. Oscillatory motion of drainage divides. Geophys Res Lett 37.
731 <https://doi.org/10.1029/2009gl040851>

732 Stock, J.D., Dietrich, W.E., 2006. Erosion of steepland valleys by debris flows.
733 Geological Society of America Bulletin 118, 1125-1148.
734 <https://doi.org/10.1130/b25902.1>

735 Stokes, M.F., Larsen, I.J., Goldberg, S.L., McCoy, S.W., Prince, P.P., Perron, J.T.,
736 2023. The Erosional Signature of Drainage Divide Motion Along the Blue Ridge
737 Escarpment. Journal of Geophysical Research: Earth Surface 128.
738 <https://doi.org/10.1029/2022jf006757>

739 Struth, L., Teixell, A., Owen, L.A., Babault, J., 2017. Plateau reduction by drainage
740 divide migration in the Eastern Cordillera of Colombia defined by morphometry
741 and ¹⁰Be terrestrial cosmogenic nuclides. Earth Surface Processes and Landforms
742 42, 1155-1170. <https://doi.org/10.1002/esp.4079>

743 Su, P., He, H., Tan, X., Liu, Y., Shi, F., Kirby, E., 2021. Initiation and Evolution of the
744 Shanxi Rift System in North China: Evidence From Low-Temperature
745 Thermochronology in a Plate Reconstruction Framework. Tectonics 40.
746 <https://doi.org/10.1029/2020tc006298>

747 Su, Q., Wang, X., Lu, H., Xie, H., 2020. Dynamic Divide Migration as a Response to
748 Asymmetric Uplift: An Example from the Zhongtiao Shan, North China. Remote
749 Sensing 12. <https://doi.org/10.3390/rs12244188>

750 Tucker, G.E., Bras, R.L., 1998. Hillslope processes, drainage density, and landscape
751 morphology. Water Resources Research 34, 2751-2764.
752 <https://doi.org/10.1029/98wr01474>

753 Tucker, G.E., Slingerland, R., 1997. Drainage basin responses to climate change.
754 Water Resources Research 33, 2031-2047. <https://doi.org/10.1029/97wr00409>

755 Vacherat, A., Bonnet, S., Mouthereau, F., 2018. Drainage reorganization and divide
756 migration induced by the excavation of the Ebro basin (NE Spain). Earth Surface
757 Dynamics, 6(2), 369-387. <https://doi.org/10.5194/esurf-6-369-2018>

758 Wang, Y., Liu, C., Zheng, D., Zhang, H., Yu, J., Pang, J., Li, C., Hao, Y., 2021.
759 Multistage Exhumation in the Catchment of the Anninghe River in the SE
760 Tibetan Plateau: Insights From Both Detrital Thermochronology and
761 Topographic Analysis. Geophys Res Lett 48.
762 <https://doi.org/10.1029/2021gl092587>

763 Waters, J.M., Craw, D., Youngson, J.H., Wallis, G.P., 2001. Genes meet geology: fish
764 phylogeographic pattern reflects ancient, rather than modern, drainage
765 connections. Evolution 55, 1844-1851. <https://doi.org/10.1111/j.0014-3820.2001.tb00833.x>

767 Wei, Z., Arrowsmith, J.R., He, H., 2015. Evaluating fluvial terrace riser degradation
768 using LiDAR-derived topography: An example from the northern Tian Shan,

769 China. *Journal of Asian Earth Sciences* 105, 430-442.
770 <https://doi.org/10.1016/j.jseaes.2015.02.016>.

771 Whipple, K.X., 2009. The influence of climate on the tectonic evolution of mountain
772 belts. *Nature Geoscience* 2, 97-104. <https://doi.org/10.1038/ngeo413>

773 Whipple, K.X., Forte, A.M., DiBiase, R.A., Gasparini, N.M., Ouimet, W.B., 2017.
774 Timescales of landscape response to divide migration and drainage capture:
775 Implications for the role of divide mobility in landscape evolution. *Journal of*
776 *Geophysical Research: Earth Surface* 122, 248-273.
777 <https://doi.org/10.1002/2016JF003973>

778 Whipple, K.X., Kirby, E., Brocklehurst, S.H., 1999. Geomorphic limits to climate-
779 induced increases in topographic relief. *Nature* 401, 39-43.
780 <https://doi.org/10.1038/43375>

781 Willett, S.D., McCoy, S.W., Perron, J.T., Goren, L., Chen, C.Y., 2014. Dynamic
782 reorganization of river basins. *Science* 343, 1117.
783 <https://doi.org/10.1126/science.1248765>

784 Willett, S.D., McCoy, S.W., Beeson, H.W., 2018. Transience of the North American
785 High Plains landscape and its impact on surface water. *Nature* 561, 528-532.
786 <https://doi.org/10.1038/s41586-018-0532-1>

787 Wobus, C., Whipple, K.X., Kirby, E., Snyder, N., Johnson, J., Spyropolou, K., Crosby,
788 B., Sheehan, D., 2006. Tectonics from topography: Procedures, promise, and
789 pitfalls, *Tectonics, Climate, and Landscape Evolution*, pp. 55-74.
790 [https://doi.org/10.1130/2006.2398\(04\)](https://doi.org/10.1130/2006.2398(04))

791 Wu, Y., Yang, R., He, C., He, J., 2022. Caution on determining divide migration from
792 cross-divide contrast in χ . *Geological Journal* 57(12),
793 <https://doi.org/10.1002/gj.4530>.

794 Xiong, L.-Y., Tang, G.-A., Li, F.-Y., Yuan, B.-Y., Lu, Z.-C., 2014. Modeling the
795 evolution of loess-covered landforms in the Loess Plateau of China using a DEM
796 of underground bedrock surface. *Geomorphology* 209, 18-26.
797 <https://doi.org/10.1016/j.geomorph.2013.12.009>

798 Xu, X., Ma, X., Deng, Q., 1993. Neotectonic activity along the Shanxi rift system,
799 China. *Tectonophysics* 219, 305-325. [https://doi.org/10.1016/0040-](https://doi.org/10.1016/0040-1951(93)90180-R)
800 [1951\(93\)90180-R](https://doi.org/10.1016/0040-1951(93)90180-R)

801 Yan, M.-J., He, Q.-Y., Yamanaka, N., Du, S., 2014. Location, Geology and Landforms
802 of the Loess Plateau, in: Tsunekawa, A., Liu, G., Yamanaka, N., Du, S. (Eds.),
803 Restoration and development of the degraded Loess Plateau, China. Springer
804 Japan, pp. 3-22. <https://doi.org/10.1007/978-4-431-54481-4>

805 Yang, R., Suhail, H.A., Gourbet, L., Willett, S.D., Fellin, M.G., Lin, X., Gong, J., Wei,
806 X., Maden, C., Jiao, R., Chen, H., 2019. Early Pleistocene drainage pattern
807 changes in Eastern Tibet: Constraints from provenance analysis,
808 thermochronometry, and numerical modeling. *Earth Planet Sc Lett* 531, 1-10.
809 <https://doi.org/10.1016/j.epsl.2019.115955>

810 Ye, Y., Tan, X., Zhou, C., 2022. Initial topography matters in drainage divide
811 migration analysis: Insights from numerical simulations and natural examples.
812 *Geomorphology* 409, 108266. <https://doi.org/10.1016/j.geomorph.2022.108266>

813 Yin, A., 2010. Cenozoic tectonic evolution of Asia: A preliminary synthesis.
814 Tectonophysics 488, 293-325. <https://doi.org/10.1016/j.tecto.2009.06.002>

815 Zemplak, T.S., Habit, E.M., Walde, S.J., Battini, M.A., Adams, E.D.M., Ruzzante,
816 D.E., 2008. Across the southern Andes on fin: glacial refugia, drainage reversals
817 and a secondary contact zone revealed by the phylogeographical signal of
818 *Galaxias platei* in Patagonia. *Molecular Ecology* 17, 5049-5061.
819 <https://doi.org/10.1111/j.1365-294X.2008.03987.x>

820 Zeng, X., Tan, X., 2023. Drainage divide migration in response to strike-slip faulting:
821 An example from northern Longmen Shan, eastern Tibet. *Tectonophysics* 848,
822 229720. <https://doi.org/10.1016/j.tecto.2023.229720>

823 Zhao, X., Zhang, H., Hetzel, R., Kirby, E., Duvall, A.R., Whipple, K.X., Xiong, J., Li,
824 Y., Pang, J., Wang, Y., Wang, P., Liu, K., Ma, P., Zhang, B., Li, X., Zhang, J.,
825 Zhang, P., 2021. Existence of a continental-scale river system in eastern Tibet
826 during the late Cretaceous-early Palaeogene. *Nat Commun* 12, 7231.
827 <https://doi.org/10.1038/s41467-021-27587-9>

828 Zhou, C., Tan, X., Liu, Y., Lu, R., Murphy, M.A., He, H., Han, Z., Xu, X., 2022a.
829 Ongoing westward migration of drainage divides in eastern Tibet, quantified
830 from topographic analysis. *Geomorphology* 402, 108123.
831 <https://doi.org/10.1016/j.geomorph.2022.108123>

832 Zhou, C., Tan, X., Liu, Y., Shi, F., 2022b. A cross-divide contrast index (C) for
833 assessing controls on the main drainage divide stability of a mountain belt.
834 *Geomorphology* 398, 108071. <https://doi.org/10.1016/j.geomorph.2021.108071>.

835 Zhou, C., Tan, X., 2023. Quantifying the influence of asymmetric uplift, base level
836 elevation, and erodibility on cross-divide χ difference. *Geomorphology* 427,
837 108634. <https://doi.org/10.1016/j.geomorph.2023.108634>

838 Zondervan, J.R., Stokes, M., Boulton, S.J., Telfer, M.W., Mather, A.E., 2020. Rock
839 strength and structural controls on fluvial erodibility: Implications for drainage
840 divide mobility in a collisional mountain belt. *Earth Planet Sc Lett* 538.
841 <https://doi.org/10.1016/j.epsl.2020.116221>